Martinez Garzon, P., Ben-Zion, Y., Abolfathian, N., Kwiatek, G., Bohnhoff, M. (2016): A refined methodology for stress inversions of earthquake focal mechanisms. - *Journal of Geophysical Research*, *121*, 12, pp. 8666—8687.

DOI: http://doi.org/10.1002/2016JB013493

AGU PUBLICATIONS

JGR

Journal of Geophysical Research: Solid Earth

RESEARCH ARTICLE
10.1002/2016JB013493

Special Section:
Stress at Active Plate Boundaries - Measurement and Analysis, and Implications for Seismic Hazard

A refined methodology for stress inversions of earthquake focal mechanisms

Patricia Martínez-Garzón[1,2], Yehuda Ben-Zion[2], Niloufar Abolfathian[2], Grzegorz Kwiatek[1], and Marco Bohnhoff[1,3]

[1]Department 4.2 Geomechanics and Rheology, Helmholtz Centre Potsdam, GFZ German Research Centre for Geosciences, Potsdam, Germany, [2]Department of Earth Sciences, University of Southern California, Los Angeles, California, USA, [3]Institute of Geological Sciences, Free University of Berlin, Berlin, Germany

Abstract We develop an improved methodology for reliable high-resolution inversions of focal mechanisms to background stress field orientation and stress ratio R in two or three dimensions. The earthquake catalog is declustered to remove events likely affected strongly by local stress interactions rather than reflecting the large-scale background stress field. The declustered data are discretized with the k-means algorithm into groups containing a number of focal mechanisms between a minimum number N_{min} and $2N_{min}$. Synthetic tests indicate that $N_{min} \approx 30$ provides stable inversion results under different stress regimes and noise conditions when $R \approx 0.5$, while $N_{min} \approx 45$ is needed for R near 0 or 1. Additional synthetic tests compare the performance of selecting the fault plane of each focal mechanism using (a) the plane with lowest misfit angle between the slip vector from the focal mechanism and shear traction from the stress tensor and (b) the plane with highest instability coefficient representing proximity to the optimally oriented fault for given stress field and friction coefficient. The instability criterion is found to provide more accurate inversion results under all tested stress regimes, stress ratios, and noise conditions. The refined inversion methodology combines selecting fault planes using the instability criterion iteratively with a damped simultaneous inversion of different focal mechanism groups. Results characterizing neighborhoods of discretized domains merged during the damped inversion provide high-resolution information independent of the discretization. Some aspects of the methodology are illustrated with focal mechanism data from the San Jacinto Fault Zone in Southern California.

Key Points:
- We present a method for deriving detailed robust information on the background stress field
- The basic building blocks are fine discretization of declustered focal mechanism data
- The results are illustrated with synthetic data and observations from the San Jacinto Fault Zone

Supporting Information:
- Supporting Information S1

Correspondence to:
P. Martínez-Garzón,
patricia@gfz-potsdam.de

Citation:
Martínez-Garzón, P., Y. Ben-Zion, N. Abolfathian, G. Kwiatek, and M. Bohnhoff (2016), A refined methodology for stress inversions of earthquake focal mechanisms, *J. Geophys. Res. Solid Earth*, *121*, 8666–8687, doi:10.1002/2016JB013493.

Received 24 AUG 2016
Accepted 13 NOV 2016
Accepted article online 15 NOV 2016
Published online 5 DEC 2016

1. Introduction

Characterization of the stress field in the brittle crust provides fundamental information on many aspects of earthquake and fault mechanics [e.g., *Zoback*, 1992; *Scholz*, 2002]. A widely used method for deriving stress field at seismogenic depths is inversion of earthquake focal mechanisms [e.g., *Michael*, 1984, 1987; *Heidbach et al*., 2010]. A number of stress inversion schemes have been developed and applied to various tectonic environments and scales [e.g., *Townend and Zoback*, 2001; *Hardebeck and Michael*, 2006; *Arnold and Townend*, 2007; *Ickrath et al*., 2015]. In the present paper we discuss several techniques for stress inversion and suggest a refined methodology for obtaining detailed and robust results. Ideally, the inversion would provide high-resolution information on natural variations of the stress field, while not being sensitive to user discretization of space and time and typical data problems. This may be achieved by (a) using fine discretization of space and time having sufficient data to provide reliable inversion results and (b) focusing on larger-scale features that characterize neighborhoods of the discretized space-time domain. One basic goal of the study is to clarify the requirements for the smallest sets of focal mechanisms that can provide robust local stress field results. Such small data sets can form the basic building blocks of a methodology that may become independent of the discretization by focusing on emerging larger-scale results.

Stress inversion results usually include the three principal stress directions and stress ratio parameter $0 \leq R \leq 1$ defined as follows:

$$R = \frac{\sigma_1 - \sigma_2}{\sigma_1 - \sigma_3} \tag{1}$$

where σ_1, σ_2, and σ_3 are the most compressive, intermediate, and least compressive principal stresses, respectively. Most algorithms inverting focal mechanisms for stress are based on the following assumptions:

1. The stress field is assumed to be homogeneous within the selected space-time domain. This is equivalent to assuming that the earthquakes used in the inversion respond to a constant stress field operating at the boundaries of the region containing the data. Since seismicity is generally clustered [e.g., *Zaliapin and*

Ben-Zion, 2013, 2016], satisfying this condition requires using declustered catalogs to remove events likely reflecting internal stress perturbations on space-time scales of the clusters rather than the entire examined space-time domain.

2. The employed earthquakes are assumed to occur along preexisting faults which have sufficiently different orientations to constrain the stress field. To perform stress tensor inversion, a number of focal mechanisms with different orientations are needed [*McKenzie*, 1969].
3. The faults are assumed to slip in the direction of the tangential traction vector. This is known as the Wallace-Bott criterion [*Wallace*, 1951; *Bott*, 1959] and can be written as follows:

$$\frac{\vec{\tau}}{|\vec{\tau}|} = \frac{\vec{s}}{|\vec{s}|}, \tag{2}$$

where $\vec{\tau}$ is the shear traction vector and $\vec{s}$ is the slip on the fault.

Because focal mechanisms have fault plane ambiguity, an additional criterion is needed to select the fault planes used in the inversion. The main differences between existing stress inversion methods are related to the inversion algorithm and handling the fault plane ambiguity. Nonlinear inversion methods generally search for a deviatoric stress tensor minimizing the cumulative rotation angle between fault planes and the stress tensor [e.g., *Gephart and Forsyth*, 1984]. The fault plane in each focal mechanism is selected to minimize the slip misfit angle β defined by

$$\cos\beta = \frac{\vec{s}\cdot\vec{\tau}}{|\vec{s}||\vec{\tau}|}. \tag{3}$$

This inversion scheme was refined by selecting the fault plane based on the relative localization of earthquake clusters or using the fault plane with the largest potential for failure according to the Mohr-Coulomb failure criterion [*Lund and Slunga*, 1999]:

$$F = \tau - \mu\sigma_n, \tag{4}$$

where τ and σ_n are the shear and normal stress components and μ is the friction coefficient. Alternatively, a linear inversion scheme developed by *Michael* [1984, 1987] additionally assumes that the magnitude of the normalized shear traction vector is close to 1 and similar from fault to fault $\left(|\vec{\tau}|\approx 1\right)$. In this case, one fault plane of each focal mechanism is selected randomly and the process is repeated with a bootstrap resampling giving uncertainty assessment [*Michael*, 1987]. This method was extended using simultaneous inversions from several spatial and/or temporal regions, and applying a damped linear inversion that produces a smooth distribution of inversion results from neighboring domains [*Hardebeck and Michael*, 2006; *Martínez-Garzón et al*., 2014]. An alternative improvement is to use an iterative approach [*Vavryčuk*, 2014], where in each iteration the stress field orientation is calculated and the fault plane with higher instability coefficient (out of the two possible in a focal mechanism) is selected for the next inversion iteration. The instability coefficient quantifies how close a fault is to an optimal orientation given a stress state and a friction coefficient and is defined [*Vavryčuk*, 2011; *Vavryčuk et al*., 2013] as follows:

$$I = \frac{\tau - \mu(\sigma - \sigma_1)}{\tau_{\text{opt}} - \mu\left(\sigma_{\text{opt}} - \sigma_1\right)}, \tag{5}$$

where subscript opt refers to optimally oriented faults.

The performance of several different stress inversion methods has been compared using synthetic tests [*Hardebeck and Hauksson*, 2001b; *Vavryčuk*, 2015]. The method of *Lund and Slunga* [1999] was found to be more accurate under different noise conditions than the inversion schemes of *Michael* [1984, 1987] and *Gephart and Forsyth* [1984]. Out of these two, the method of *Michael* [1984, 1987] provided more accurate uncertainty estimates than *Gephart and Forsyth* [1984], especially under noisy conditions. However, a number of important choices on selecting focal mechanisms for the inversion are frequently made semiarbitrarily and can lead to spurious results. These include how many focal mechanisms and of what diversity should be inverted. In addition, the assumption on stress homogeneity may not be fulfilled when mixing seismicity from different sides of a fault zone or across several domains with different deformation patterns. As

mentioned, using regular earthquake catalogs with clustered seismicity is also not consistent with stress homogeneity in the examined domain. These factors may affect the stress inversion results as much as the choice of the inversion method or even more.

In the following sections we develop a refined stress inversion methodology, with particular emphasis on data selection and space-time discretization, to accurately determine the background stress field in regions of two or three dimensions. The various steps of the methodology are summarized in Figure 1. The minimum number of focal mechanisms that can provide stable inversion results is investigated using synthetic tests. Effects of using regular (nondeclustered) catalog on stress inversion results are demonstrated with data from the San Jacinto Fault Zone (SJFZ) in Southern California. Our proposed methodology uses declustered catalogs to obtain the background stress field distributions in the analyzed domain. An objective and automatized technique is provided for grouping the focal mechanisms into inversion data sets according to the Cartesian distance between events. While inverting for stress, we investigate which criterion for selecting the fault plane has the largest success with synthetic tests. Finally, we combine the iterative scheme and the damped least squares inversion, allowing for an improved resolution of two- or three-dimensional stress maps. We illustrate the performance of the methodology with synthetic tests and seismic data from the SJFZ.

2. Data

Some parts of the proposed methodology are developed using synthetic tests with known initial stress conditions, while others are illustrated using observed earthquake data. The various used data sets are described below.

2.1. Synthetic Tests

We create different subsets of focal mechanisms satisfying constant stress field orientation and given stress ratio. We test three different stress field orientations corresponding to the three Andersonian regimes (normal, strike-slip, and reverse faulting). Results for stress ratio $R = 0.5$ corresponding to each of these regimes are illustrated in the main text, while results of tests with $R = 0.1$ and $R = 0.9$ (representing mixed regimes or cases where the faulting style may change from one type to another) are provided in the supporting information. For each assumed stress regime, 500 synthetic focal mechanisms are generated using the approach of *Vavryčuk* [2015]. Strike and dip are selected randomly from the range of allowed fault orientations in a Mohr circle associated with a given failure criterion. The rake is calculated using the Wallace-Bott criterion (equation (2)).

We analyze noise-free synthetic focal mechanisms, as well as mechanisms with fault plane parameters having added random noise to account for observational errors. The noise is added by perturbing independently the three parameters defining the fault geometry (strike, dip, and rake) with a uniform random value up to threshold levels from 5° up to 40°. Alternative methods to simulate measurement uncertainties, such as perturbing the slip vectors and modifying the mechanisms by a certain 3-D rotation angle, have been previously tested [e.g., *Martínez-Garzón et al*., 2016]. The method used here for perturbing the fault plane parameters was selected because it modifies the focal mechanisms more uniformly along the three stress regimes analyzed, while maintaining double-couple sources. To stabilize the solutions of the stress inversion and achieve representative results for each case of assumed fault plane uncertainty, we create and invert 50 different realizations of the focal mechanisms with different uncertainties and stack the corresponding stress inversion results. An example of the improvement and increased stability of stacked solutions compared to one stress realization is provided in Figure S1 in the supporting information. In the main synthetic tests, the fault plane ambiguity is addressed by selecting as in *Vavryčuk* [2014, 2015] the plane with higher instability coefficient (equation (5)).

2.2. Seismicity Catalogs From a Fault Zone

To illustrate parts of our stress inversion methodology, we also use seismicity from the San Jacinto Fault Zone. The SJFZ is the most seismically active fault zone in Southern California and is characterized by significant complexity of structures and focal mechanisms [e.g., *Bailey et al*., 2010; *Allam and Ben-Zion*, 2012]. We use data that occurred in 2010 in the highly active trifurcation area of the SJFZ and the region to the NW. The year 2010 is chosen because of the increased seismicity rates in Southern California after the 4 April 2010 M_w 7.2 El Mayor-Cucapah earthquake [e.g., *Meng and Peng*, 2014], and the occurrence of two earthquakes with local

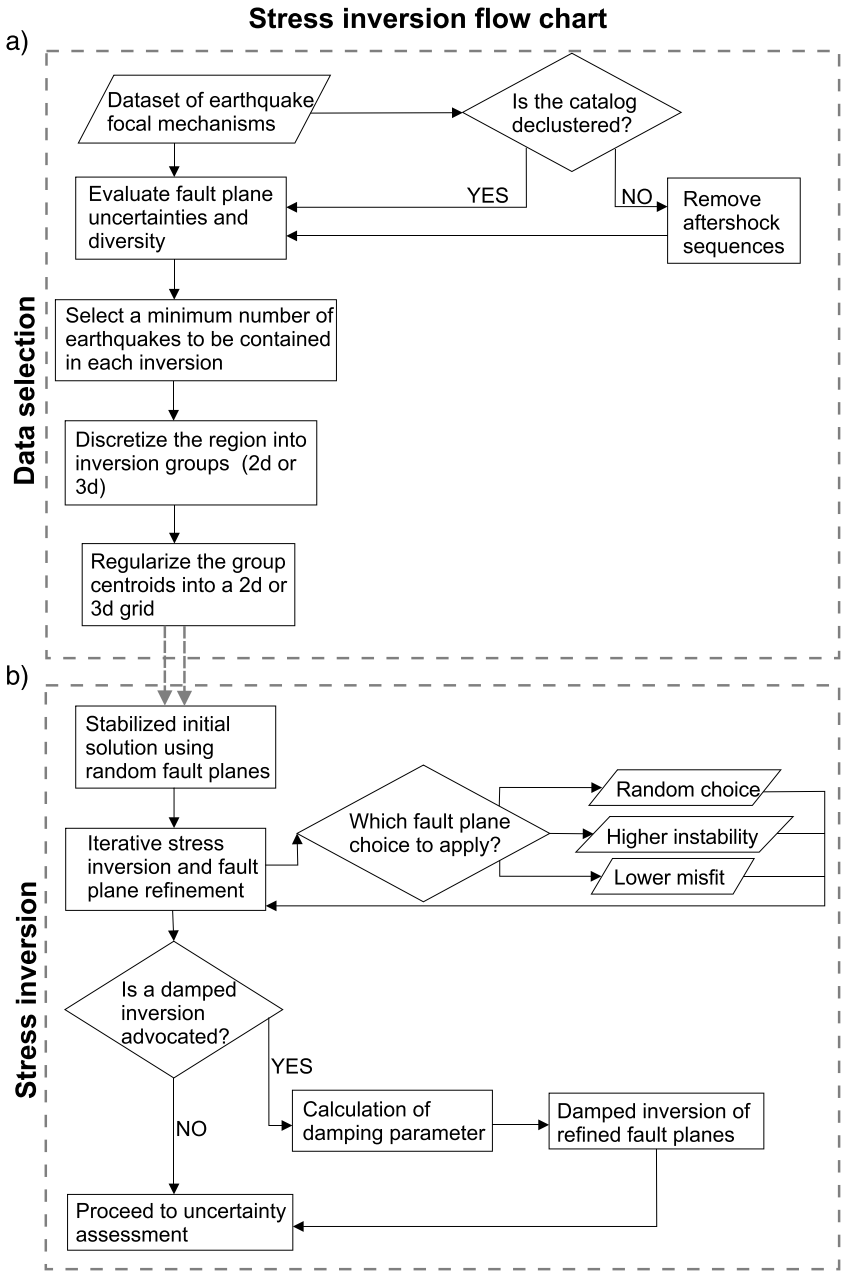

Figure 1. Flowchart summarizing the different steps composing (a) the data selection and (b) the stress tensor inversion from focal mechanisms.

magnitudes M_L 4.3 and 5.4 in the trifurcation area. Earthquake hypocenters and focal mechanisms for the analysis are taken from the relocated seismicity catalog of *Hauksson et al.* [2012] and *Yang et al.* [2012], respectively. The seismicity catalog has 5366 events within the selected region and time period, of which 3373 have focal mechanisms.

As mentioned, using declustered rather than full catalogs is more consistent with one of the basic assumptions of typical stress inversion methods. To get a declustered catalog, we separate the seismicity to background events and clusters using the approach and parameters of *Zaliapin and Ben-Zion* [2013] but estimating spatial distances with hypocenters rather than epicenters. The declustered catalog consists of the background events, which include the first earthquake in each cluster. If the first event in a cluster does not have a focal mechanism that can be used for the stress inversion, we replace it with a later event up to the main shock. For some applications one may also include the foreshocks part of clusters to increase the data,

but this is not done here. In most analyses done in this study, out of the 5366 events comprising the original catalog in the examined space-time domain, 2139 remain in the declustered catalog, of which 1376 have focal mechanisms. Section 3.2 illustrates inferred temporal changes in a smaller region around the trifurcation area based on original and declustered catalogs with 2460 initial events and 660 focal mechanisms, respectively.

3. Data Selection for Stress Inversion

Appropriate data selection and processing of the focal mechanisms is crucial for obtaining high-resolution robust results on properties of the stress field. In this section we discuss and illustrate three main aspects of data selection: the minimum number of events providing reliable inversion results, the use of declustered earthquake catalogs, and the discretization of space and time with data to be inverted (Figure 1a).

3.1. Required Number of Focal Mechanisms per Inversion

Earthquakes occur on faults having a range of orientations with respect to the regional stress field [e.g., *Sibson*, 1985], so a single focal mechanism (i.e., the *P* and *T* axes) is not sufficient to estimate the background stress [*McKenzie*, 1969]. The focal mechanism data used in stress inversions should sample the diversity of focal mechanisms consistent with a given stress field. We perform synthetic tests to evaluate the accuracy of retrieved principal stress orientations and stress ratio with different data sets. In each test we use between 5 and 200 mechanisms that sample uniformly the range of fault orientations consistent with the assumed stress field (section 2.1). The difference between the assumed and retrieved orientation of the principal stress axes is measured by the 3-D rotation angle ($0° \leq \gamma \leq 120°$) between the stress tensors [*Kagan*, 1991].

Results from stress inversions selecting the fault plane with the instability criterion (equation (5)) and $R = 0.5$ show that the stress field orientation can be resolved with similar accuracy regardless of the stress regime (Figure 2a). For data with noise up to 20°, stacked results of 50 realizations indicate that a minimum of 20 focal mechanisms is necessary to retrieve the stress field orientation with accuracy of $\gamma < \pm 10°$. Similarly, for data sets containing 40° noise, a minimum of 40 focal mechanisms is needed to resolve the stress field orientation with similar accuracy. The stability of the results may be inferred from the standard deviation of the distribution of 3-D rotation angles γ associated with the different (50) realizations (Figure 2b). The stress ratio appears similarly constrained for the strike-slip and reverse stress regimes, and the same number of focal mechanism mentioned above is necessary to constrain it within ± 0.1 (Figures 2c and 2d). However, under normal faulting regime cases with relatively large focal mechanism uncertainties are found to significantly decrease the accuracy of the inverted *R* value.

Hardebeck and Hauksson [2001b] estimated that a focal mechanism diversity of 30°–45° is needed to constrain the stress field orientation. Here we evaluate the focal mechanism diversity included in each of the synthetic stress inversions from the mean of the 3-D rotation angles [*Kagan*, 1991] between all pairs of focal mechanisms used in the inversion (similar results are obtained using medians instead of means). In the synthetic tests assuming $R = 0.5$, the fault plane diversity in all three analyzed stress regimes varies from ≈ 30° for noise-free data (genuine fault plane diversity) to ≈ 65° for data sets with up to 40° noise. The latter represents an apparent diversity combining the genuine fault plane diversity and the added observational errors (Figures 3a and 3b). The standard deviations of γ from different noise realizations decrease with increasing number of focal mechanisms. However, these tests suggest that including >60 focal mechanisms in an inversion does not significantly improve the accuracy of either the stress field orientation or the stress ratio.

The slip misfit angle β (equation (3)) can be used to evaluate the accuracy of the inversion or alternatively the consistency of the focal mechanisms with the derived stress field [*Michael*, 1991]. The rake in the synthetic tests is calculated according to equation (2), so the obtained β values should reflect the noise level included in each data set. Indeed, for focal mechanisms with 20° noise the mean slip misfit angles is approximately 15°, while mechanisms with 40° noise lead to mean β values of about 40° (Figure 3c). This may not necessarily be the case with observed focal mechanisms, since the slip orientation of some earthquakes may differ from the shear traction predicted from the stress field.

Equivalent synthetic tests with extreme stress ratios of $R = 0.1$ and $R = 0.9$ representing mixed or transitional stress regimes show that recovering accurately the stress field orientation in these cases requires inversion of data sets with larger number of focal mechanisms (Figures S2 and S3). If the mechanisms have about 20° noise or more, the inverted stress orientation may have a significant error. However, using the fault instability

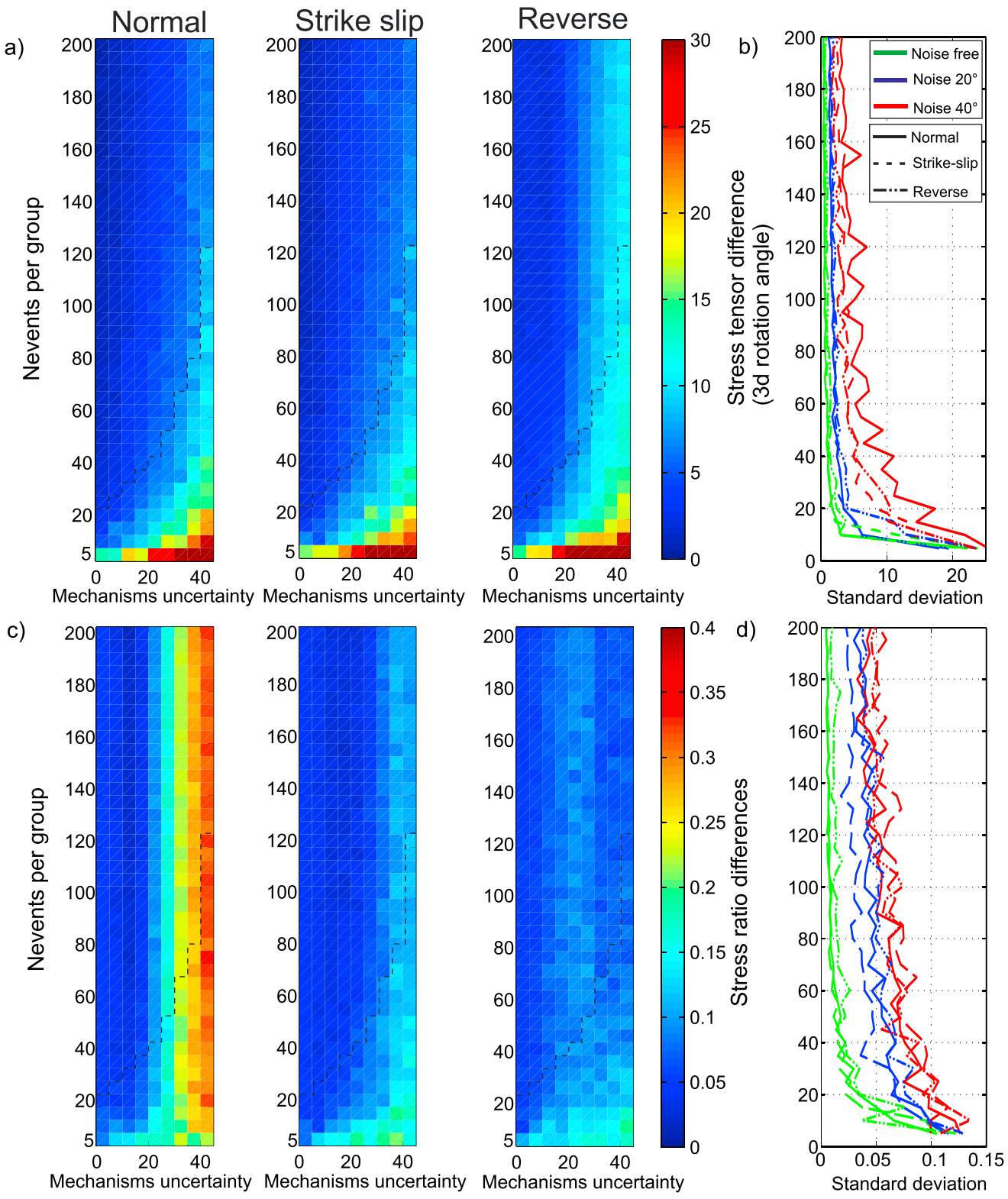

Figure 2. (a) Rotation angle between imposed and retrieved deviatoric stress tensors for normal, strike-slip, and reverse stress regimes as a function of focal mechanism uncertainties and number of events per group. (b) Standard deviations of rotation angles obtained from inversions of noise-free focal mechanisms (green lines), 50 realizations with 20° mechanisms uncertainty (blue lines), and 50 realizations with 40° uncertainty (red lines). (c) Differences between imposed $R = 0.5$ and retrieved R value for the normal, strike-slip, and reverse stress regimes. (d) Same as Figure 2b for stress ratio differences. Black dashed lines in Figures 2a and 2c represent approximate minimum number of events per group beyond which the accuracy of the inversion results does not change significantly.

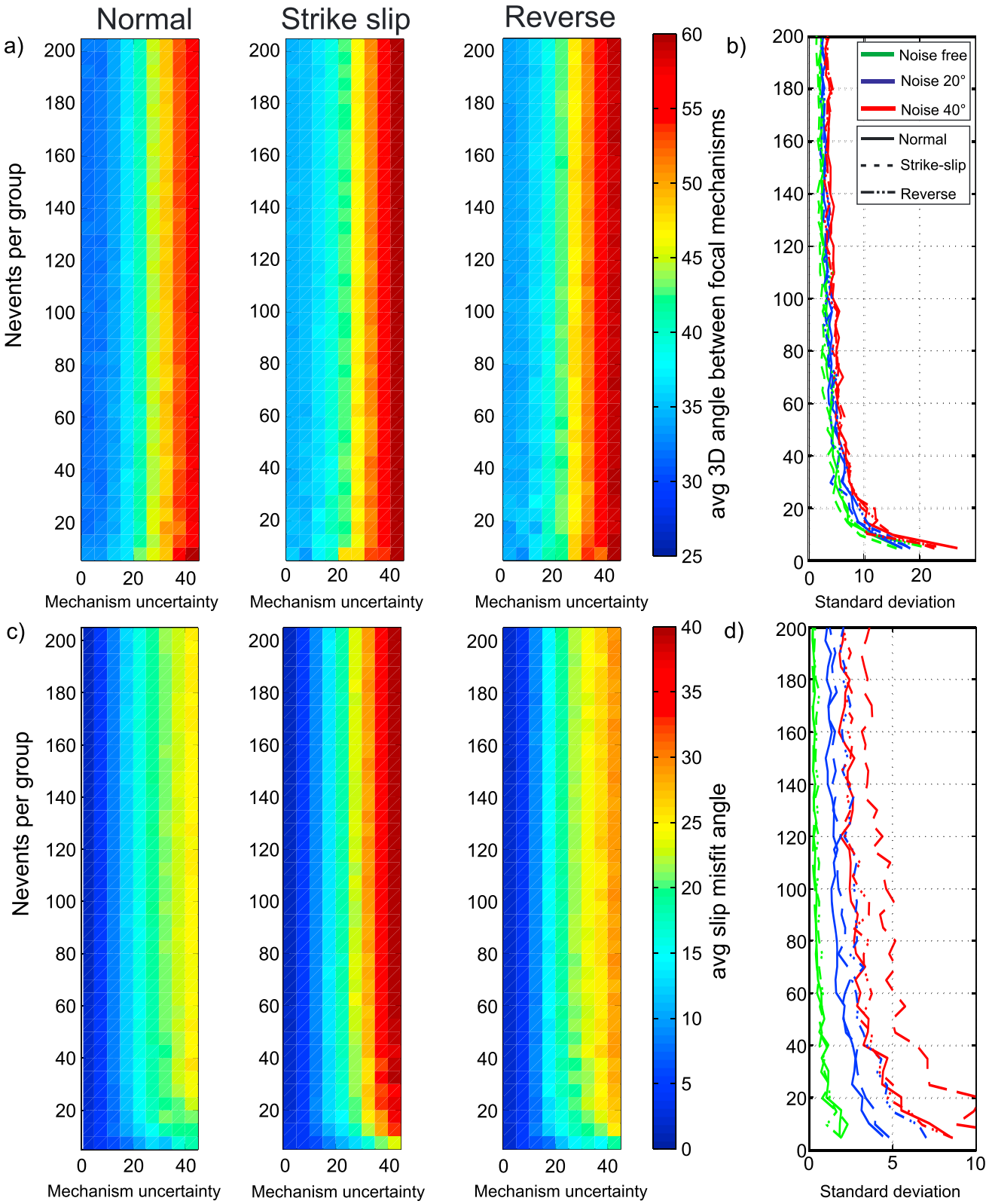

Figure 3. (a) Average 3-D rotation angle between pairs of focal mechanisms used in each stress inversion as a function of event number per group and focal mechanism uncertainties. (b) Standard deviations of the 3-D angles obtained from inversions of noise-free focal mechanisms (green lines), 50 realizations with 20° mechanisms uncertainty (blue lines), and 50 realizations with 40° uncertainty (red lines). (c) Average misfit angle β between each of the focal mechanisms from a group and the inverted deviatoric stress tensor. (d) Same as Figure 3b for β.

criterion to select the fault planes, the stress ratios are recovered as accurately as in the test with $R = 0.5$ regardless of the noise level and independently of whether the stress orientation was retrieved correctly or not. The focal mechanism diversity in the tests with $R = 0.1$ and $R = 0.9$ substantially increases reaching $\approx 60°$ for noise-free data. These cases facilitate fault failures consistent with two stress regimes, resulting in an increased range of orientations (Figures S4 and S5).

In summary, if the focal mechanisms sufficiently cover the range of allowed orientations within a stress field, in environments with a stress ratio $R \approx 0.5$ at least 20 mechanisms are necessary to resolve the stress field orientation with low noise conditions, while at least 40 are necessary for data sets with high noise. If the genuine fault plane diversity is smaller than the values used in the tests, the retrieved stress tensor may not be properly constrained by the data. The synthetic tests also indicate that there is a correlation between the diversity of fault mechanisms and noise level in the data, resulting in larger apparent diversity for focal mechanisms with larger uncertainties. Inverting a larger number of focal mechanisms than suggested by the dashed boundary lines in Figure 2 may not significantly improve the results, while reducing the resolution of the inverted results.

3.2. Use of Declustered Catalogs

It is well known that earthquakes redistribute the stress released in the failure area to the surrounding region [e.g., *Okada*, 1985; *Ben-Zion and Rice*, 1993; *King et al*., 1994]. In particular, aftershocks are strongly influenced by the stress transfer from main shocks, and not necessarily driven primarily by the background stress field as assumed in typical stress inversions. Several studies have reported stress rotations after the occurrence of large earthquakes [e.g., *Hardebeck and Hauksson*, 2001a; *Bohnhoff et al*., 2006; *Wesson and Boyd*, 2007], but they included aftershocks when inverting for the stress. In such cases the observed changes in the stress regime may be related to changes in the background stress field, variations produced by local stress transfers within event clusters, or a mixture of both types of changes.

Hardebeck [2010] concluded that the aftershocks of the 1992 Landers earthquake are well aligned with the background stress field, but this may not necessarily characterize all the events or hold for other cases. *Ross and Ben-Zion* [2013] reported on spatiotemporal variations in rotation angles of double-couple mechanisms of Landers aftershocks, especially early after the Landers event and near the rupture end. To analyze spatial or temporal distributions of background stress field, it is preferred to use declustered seismicity and eliminate events which may be strongly affected by local stress perturbations. Below we illustrate with analysis of observed data temporal stress variations likely related to internal interactions within earthquake clusters rather than reflecting large-scale changes characterizing the entire examined domain. This is done using earthquakes from the year 2010 near the trifurcation area of the SJFZ (Figures 4a and 4b). We process the complete and declustered seismicity catalogs with a similar approach and invert the focal mechanisms for stress field parameters. We divide the seismicity into moving temporal windows of 60 focal mechanisms shown in section 3.1 to provide sufficient data for accurate inversion of the stress parameters. The moving temporal windows overlap by 30 events.

We perform damped stress inversions [*Hardebeck and Michael*, 2006] that provide smooth output of temporal variations on timescales which depend on the damping parameter (selected to be 2.4 for both inversions) and are larger than those associated with the discretization of time (60 events here). The instability criterion of equation (5) [*Vavryčuk*, 2014] is used to select a more likely fault plane of each focal mechanism. The analysis of both seismicity catalogs reveals an overall strike-slip faulting regime with overall similar principal stress orientations and R values. However, the occurrence of the two largest earthquakes (M_L 4.9 and 5.5 around June 2010) produce in the analysis of the complete catalog substantial stress changes reflected in plunge changes of the σ_1 and σ_2 stress axes up to 15° as well as changes in the stress ratio (Figures 4c–4e). These rapid temporal stress changes are absent in the results of the declustered catalog (Figure 4, right column), suggesting that the background stress was not significantly modified by the occurrence of the M_L 4.9 and 5.5 earthquakes.

Figure 5 presents differences in the mean 3-D rotation angles between all pairs of focal mechanisms in the complete and declustered seismicity in subregions consisting of 5 km × 5 km squares. Depending on the location, the average fault plane diversity may increase or decrease by declustering the catalog. The differences between the focal mechanism diversity in the two catalogs is largest around the trifurcation area, where the

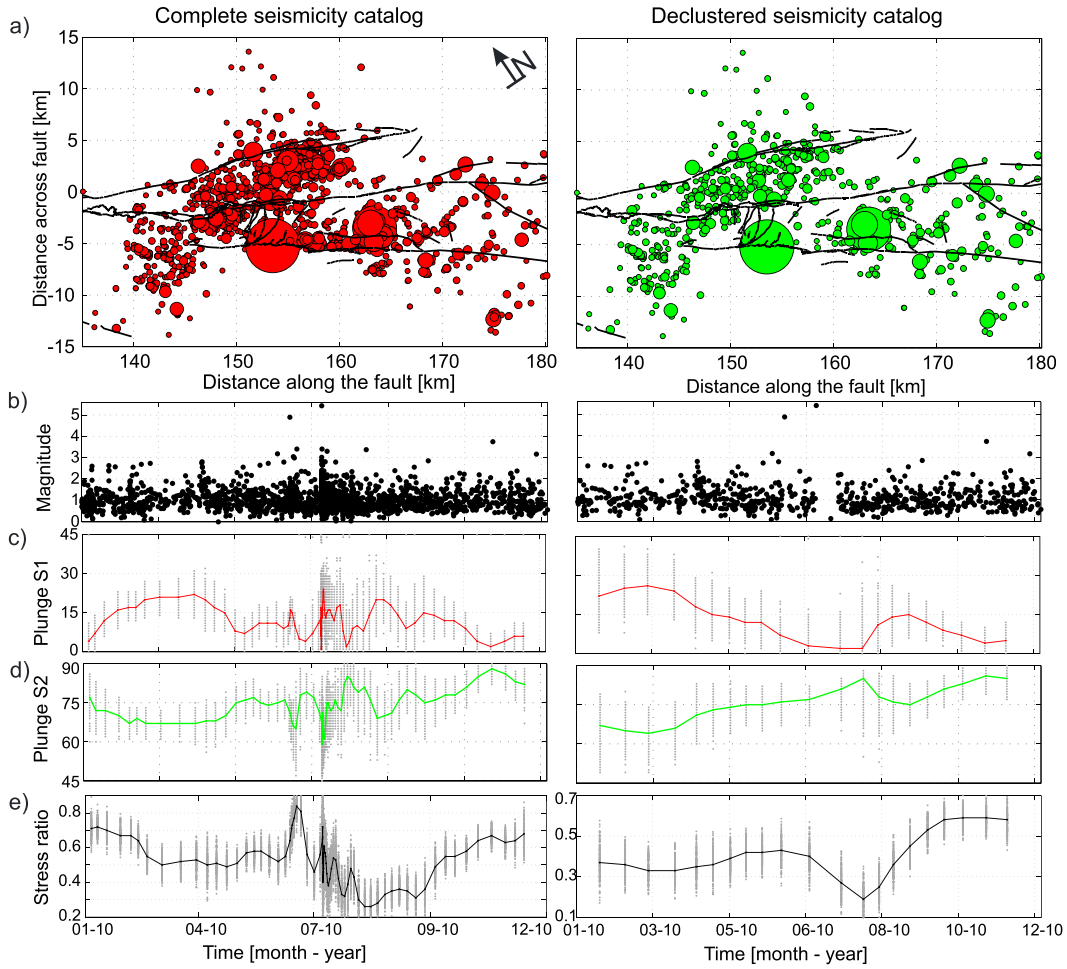

Figure 4. Differences in stress inversion results using (left column) complete and (right column) declustered seismicity in year 2010 around the trifurcation area of the San Jacinto Fault Zone. (a) Spatial distribution of the analyzed seismicity with symbol size proportional to the magnitude M_L. Black lines represent mapped surface fault traces. (b) Temporal distribution and M_L values of the seismicity from each catalog. (c) Temporal evolution of the plunge angles of the most compressive stress σ_1. (d) Same as Figure 4c for the intermediate stress σ_2. (e) Temporal evolution of the inverted stress ratio R. Grey dots in Figures 4c–4e represent 95% confidence interval from bootstrap resampling.

larger magnitude earthquakes occurred (Figure 5). This indicates that the seismicity clusters associated with these larger events have larger focal mechanism diversity than the background seismicity. A well-documented example of increased focal mechanism diversity in an aftershock sequence is associated with the 1989 Loma Prieta earthquake [*Michael*, 1990; *Michael et al.*, 1990]. As shown in Figure 5, in some cases removing the aftershocks may also lead to larger average 3-D rotation angle. Using a declustered catalog may not always significantly modify the inversion results, depending on the level of event clustering present at the data. However, using a declustered catalog is generally more consistent with the stress inversion assumptions (at a price of some data reduction).

3.3. Grouping of the Seismicity

Different data discretization methods can affect the inverted stress field orientations and result in discrepancies in the interpretation of related physical models [e.g., *Hardebeck and Hauksson*, 1999; *Townend and Zoback*, 2001; *Hardebeck and Michael*, 2004]. Despite its importance, the discretization of seismicity for analysis of stress field orientations is frequently done arbitrarily, e.g., inverting seismicity contained in regions of fixed dimensions [*Ickrath et al.*, 2015]. The subjectivity of such procedures may be reduced by comparing the stress field orientations obtained by grouping the seismicity into regions of different dimensions [e.g., *Yang and Hauksson*, 2013], or using a damped stress inversion aiming at reducing potential artifacts related to data discretization [*Hardebeck and Michael*, 2006].

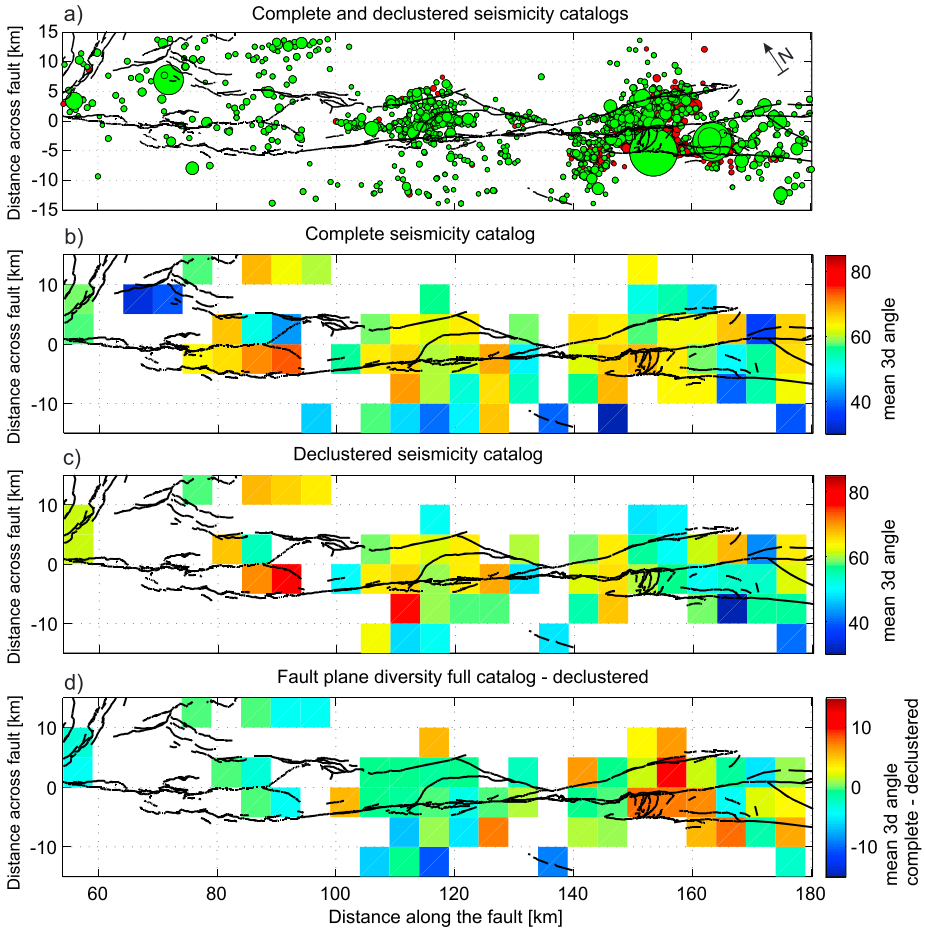

Figure 5. (a) Subset of seismicity along the SJFZ during the year 2010. Green color events represent main shocks, while red events represent either aftershocks or foreshocks. Average 3-D angle between pairs of focal mechanisms contained within regions of 5 km × 5 km using a (b) complete and (c) declustered seismicity catalog. (d) Differences in the mean 3-D angles between focal mechanisms from the same region using complete and declustered catalogs in each discretized region.

In this section we propose an objective method for discretizing the seismicity catalog in space and/or time into groups to be used by the stress tensor inversion. This method only depends on the minimum number of focal mechanisms that can provide robust estimations of the stress field orientation and stress ratio. To discretize the seismicity catalog, we use iteratively a *k*-means optimization grouping algorithm that divides the seismicity into a predefined number of groups [*Hartigan and Wong*, 1979; *Seeber*, 1984]. In each iteration of the *k*-means algorithm, each earthquake is assigned to the group with the nearest centroid. The algorithm minimizes a squared error function defined as follows:

$$J = \Sigma_{j=1}^{k} \Sigma_{i=1}^{n} \left\| x_i^{(j)} - c_j \right\|^2, \tag{6}$$

where x represents the position of the i earthquake and c is the position of the j nearest group centroid. Potential changes in the stress field orientation are assumed to occur in localized volumes in space and/or time. Cartesian squared Euclidean distance $d(x, c)$ is used to create groups of focal mechanisms from the seismicity catalog. The distances between pairs of events can be chosen to represent either epicentral or hypocentral locations and they can be normalized, e.g., to include the time as an additional dimension to group the seismicity. When the distances are not normalized, the resulting regions are equivalent to the application of centroidal Voronoi tessellation [*Voronoi*, 1908]. The methodology has the following steps:

1. From the total number of focal mechanisms of a catalog N_{tot}, select a minimum number of focal mechanisms N_{min} to be included in each group.

2. The *k*-means grouping algorithm is executed for a number of trials to test the splitting of the catalog into a number of groups between 2 and N_{tot}/N_{min}. In each trial, the average silhouette coefficient [*Rousseeuw*, 1987] describing the similarity of an earthquake to its own assigned group is calculated.
3. Choose the splitting of the catalog into a number of groups N_{group} providing the largest average silhouette coefficient. Depending on N_{tot}, the average number of events included in each of the resolved groups may be substantially larger than the desired N_{min}. Each of the obtained groups containing a number of earthquakes $N_{group} > 2N_{min}$ is subdivided iteratively into a number of new groups between 2 and $N_{group}/2N_{min}$.
4. Among these new trials of splitting each of the obtained groups, the splitting providing the largest number of "acceptable" groups (with a number of events between N_{min} and $2N_{min}$) and maximizing the number of earthquakes used in the groups is chosen. The obtained groups thus contain a number of focal mechanisms ranging between N_{min} and 2 N_{min}.

Although the seismicity catalog is usually discretized into smaller groups than those suggested by the largest average silhouette coefficient, the further subdivision is performed preserving that structure, i.e., not mixing earthquake populations separated by the best splitting. As an alternative algorithm to group the seismicity, we also investigated a hierarchical algorithm based on the degree of linkage between events [*Jonhson*, 1967]. This algorithm can also provide suitable earthquake groups to be inverted for the stress tensor. However, the number of earthquakes per group is less uniform than using the outlined *k*-means algorithm, resulting in an increased number of rejected earthquakes from groups composed of less data than the assumed N_{min}.

To illustrate the performance of the discretization algorithm, we apply it to the declustered seismicity catalog from the central portion of the SJFZ (see section 2.2 for details). The normalized epicentral coordinates of events are used to compute the Cartesian distance between earthquakes (i.e., we discretize the seismicity in 2-D). Using $N_{min} = 30$, as suggested by the synthetic results in section 3.1, produces groups containing between 30 and 60 focal mechanisms. The discretization of the catalog with the largest mean silhouette coefficient generates seven groups containing between 57 and 470 earthquakes (Figure 6a). The seismicity is not clearly separated in space, but the event groups appear generally well delimited by the main fault traces although they are not explicitly included in the grouping. In the next step, the groups from the highest silhouette coefficient are further divided into smaller subgroups to achieve the desired range of focal mechanisms number per group. This leads to 30 groups containing between 30 and 60 events, which together enclose 92% of the seismicity included in the declustered catalog (Figure 6b). The individual groups are well divided by the main fault traces in the region, confirming that the method is effectively finding optimum earthquakes groups that can be used for resolving the stress field orientation in detail. Some of the groups cover larger areas than most groups because of the uneven spatial density of the seismicity.

4. Stress Inversion

Once the focal mechanisms are selected and discretized, they can be inverted for the stress field orientation (Figure 1b). To apply existing stress inversion codes, we first reassign the groups of focal mechanisms into a regular grid. We then investigate the performance of two different criteria to select the correct fault plane from the focal mechanisms. Finally, we apply an updated stress inversion benefitting from recent inversion techniques.

4.1. Conversion to a Regular Grid

A well-established stress inversion method is the SATSI damped technique [*Hardebeck and Michael*, 2006]. In this method, a scalar damping factor *d* reduces the differences in the orientation of principal stress axes and stress ratio between neighboring groups. To use this procedure, we map the groups of irregularly distributed events produced by the *k*-means algorithm (section 3.3) to a regular grid by assigning the centroid of each group to the nearest grid node. To find the optimum regular grid fitting the obtained groups, we test all possible grid configurations between a 2×2 ($\times 2$) and a maximum provided [x_{max}, y_{max}, (z_{max})]. For each of these grid configurations, each group centroid is assigned to the nearest node of coordinates *x*, *y*, *z*. If a grid node is assigned more than one group centroid, the grid configuration is rejected; otherwise, the configuration is accepted. From all accepted configurations, the one with the largest number of occupied neighbors is selected. Applying this regularization technique to the discretized groups of focal mechanisms from the SJFZ produces a 2-D grid of 53×4 (Figure 7a) having a total of 38 occupied neighbors (Figure 7b).

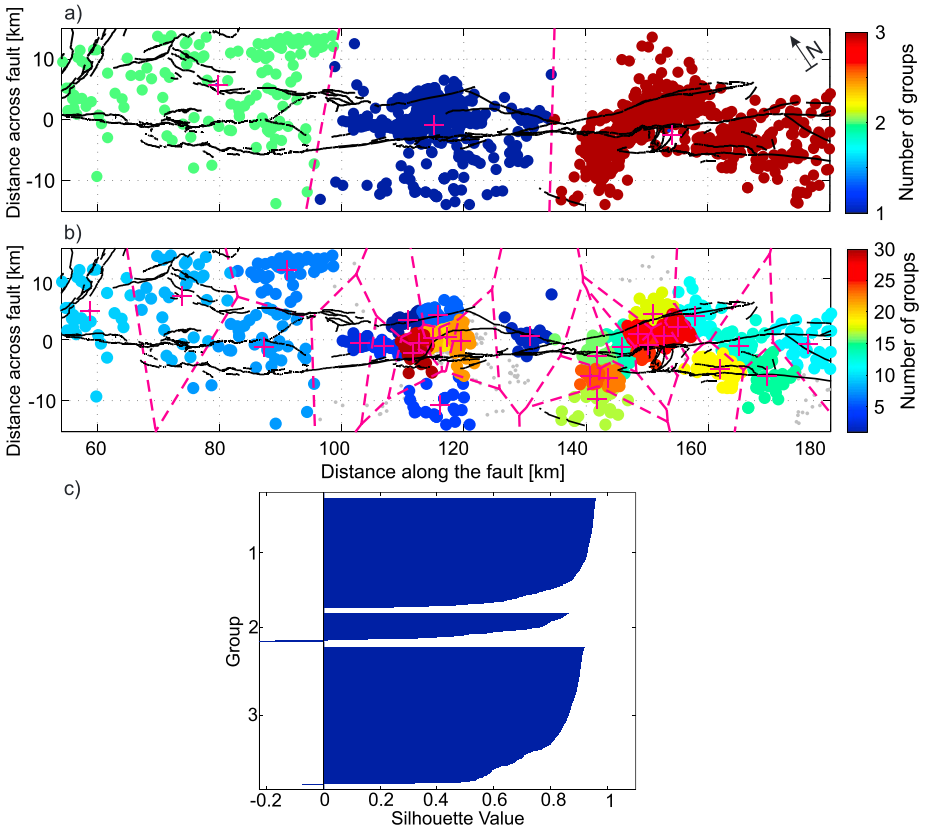

Figure 6. Map view of analyzed seismicity along the SJFZ. Filled circles represent the seismicity, and colors denote the different resolved groups after applying the discretization technique (see text for details). (a) Initial groups corresponding to the largest silhouette coefficient. (b) Final groups further subdivided and preserving the preferred discretization shown in Figure 6a with the largest silhouette coefficient. Black lines represent surface fault traces. Dashed pink lines represent the Voronoi cells. Pink crosses denote the centroid of the groups. Small grey dots in Figure 6b represent seismicity not included in the selected groups. (c) Silhouette coefficients of the different groups obtained with the best data splitting.

4.2. Addressing the Fault Plane Ambiguity

In the synthetic stress inversion tests, the correct fault plane of each focal mechanism is known. Here we investigate the success of choosing the correct fault plane in the synthetic tests described in section 2.1 according to two different criteria: (i) the fault planes with the largest instability coefficient I (equations (4) and (5)) in a given stress field [e.g., *Lund and Slunga*, 1999; *Vavryčuk*, 2014] and (ii) the fault planes with the lowest slip misfit angle β (equation (3)) in a given stress field [e.g., *Gephart and Forsyth*, 1984].

The obtained rates of success in picking the correct fault plane with each criterion show that the main factor controlling the success of these criteria is the noise level contained in the focal mechanisms, with the largest success obtained at reduced noise conditions (Figure 8). For the performed tests assuming $R = 0.5$, the instability criterion displays larger success than the slip misfit angle criterion. The standard deviation of the fraction of correctly picked fault planes in the 50 noise realizations is used to evaluate the stability of the performance. For tests assuming $R = 0.5$, the instability criterion has also more stable results (Figures 8b and 8d). Remarkable differences in the performance of the criteria are observed under reverse stress regime. Using the fault instability criterion, the fraction of correctly picked fault planes under reverse stress regime is lower than under normal or strike-slip stress regimes. Moreover, the lowest slip misfit angle criterion fails to pick the correct fault planes in a reverse stress regime regardless of the noise levels (Figures 8a and 8c). Despite of this, the final stress field orientation is still similar to the imposed stress regime, demonstrating the general stability of the stress inversion regardless of the selected fault planes. The performance of the fault plane criteria in cases with extreme values of R ($R = 0.1$ and $R = 0.9$) is shown in Figures S6 and S7. In these cases, the instability criterion is nearly as effective as with $R = 0.5$, while the slip misfit angle criterion has higher failure rate. These results are in agreement with the previous synthetic tests of *Lund and Slunga* [1999].

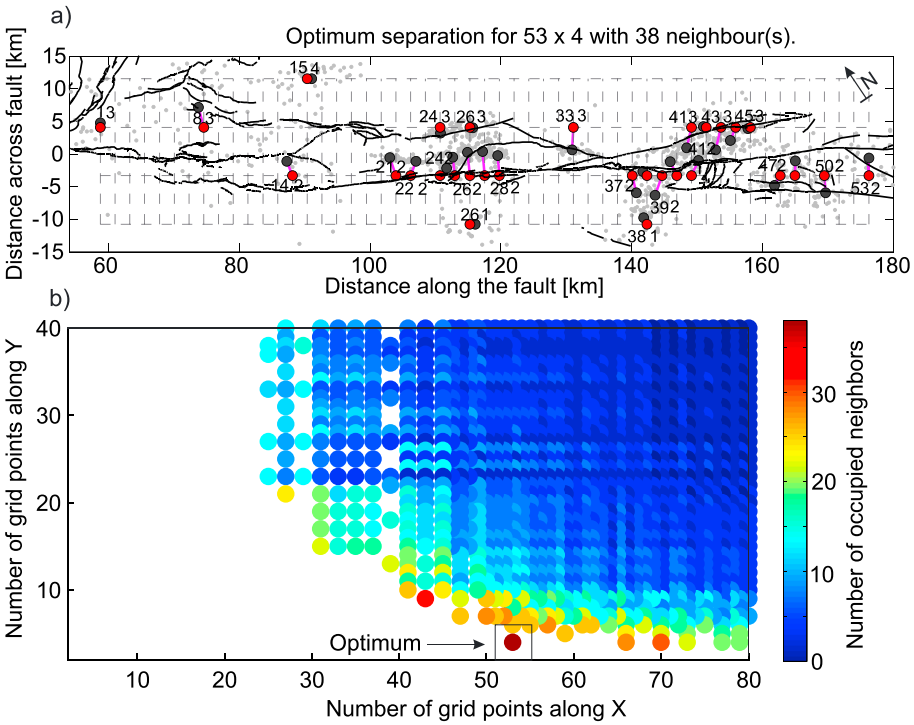

Figure 7. Distribution of the earthquake groups in a regular 2-D grid used by the SATSI [*Hardebeck and Michael*, 2006] and MSATSI [*Martínez-Garzón et al.*, 2014] stress inversion techniques. (a) Optimum regular gridding of the focal mechanism groups from the SJFZ. Dark grey circles represent the centroids of the earthquake groups. Red circles represent their corresponding mapping onto a regular 2-D grid. Grey numbers beside the points represent the *x, y* coordinates of the grid node. Light grey dots denote individual earthquakes. (b) Number of occupied neighbors in each of the tested regular grid configurations. The grid selected is the one with the largest number of occupied neighbors.

4.3. Stress Inversions

Our proposed stress inversion scheme integrates ingredients discussed in earlier sections with existing inversion procedures. The linear damped least squares inversion [*Hardebeck and Michael*, 2006] is commonly used to map the stress field orientation and stress ratio in two or three dimensions. A version of this technique allowing for quicker use [*Martínez-Garzón et al.*, 2014] is merged here with an iterative stress inversion for selecting the fault planes with the instability criterion as described above [*Vavryčuk*, 2014]. These ingredients are merged using the following steps (Figure 1b):

1. Create focal mechanism groups from the declustered seismic data and assign them into a regular grid configuration.
2. As in *Vavryčuk* [2014, 2015], invert the stress field orientation for a number of realizations without damping (i.e., each group is inverted independently) and random selection of fault planes. Use the stacked normalized solution from the different realizations as an initial deviatoric stress tensor.
3. Perform an iterative stress inversion technique similar to the approach of STRESSINVERSE [*Vavryčuk*, 2014] but extended to be applied to all groups concurrently. In each iteration, the fault planes are chosen according to the highest instability (this can be replaced with another criterion), and the process is repeated until the results in subsequent iterations do not change by more than ≈ 5%; typically, only a few iterations (e.g. ≈5) are needed to get stable results.
4. If the results do not exhibit variations on the scale of the employed discretization, they are taken as the final product of the inversion to preserve high-resolution information. Alternatively, if there are variations on the discretization scale, perform with the chosen fault planes a damped stress inversion as in SATSI [*Hardebeck and Michael*, 2006] and MSATSI [*Martínez-Garzón et al.*, 2014] to reduce differences of stress orientations and ratios between neighboring groups of events.
5. Estimate uncertainties for the orientation of the principal stress axes and stress ratios following the design of SATSI by random bootstrap resampling of the fault planes [*Michael*, 1987; *Hardebeck and Michael*, 2006].

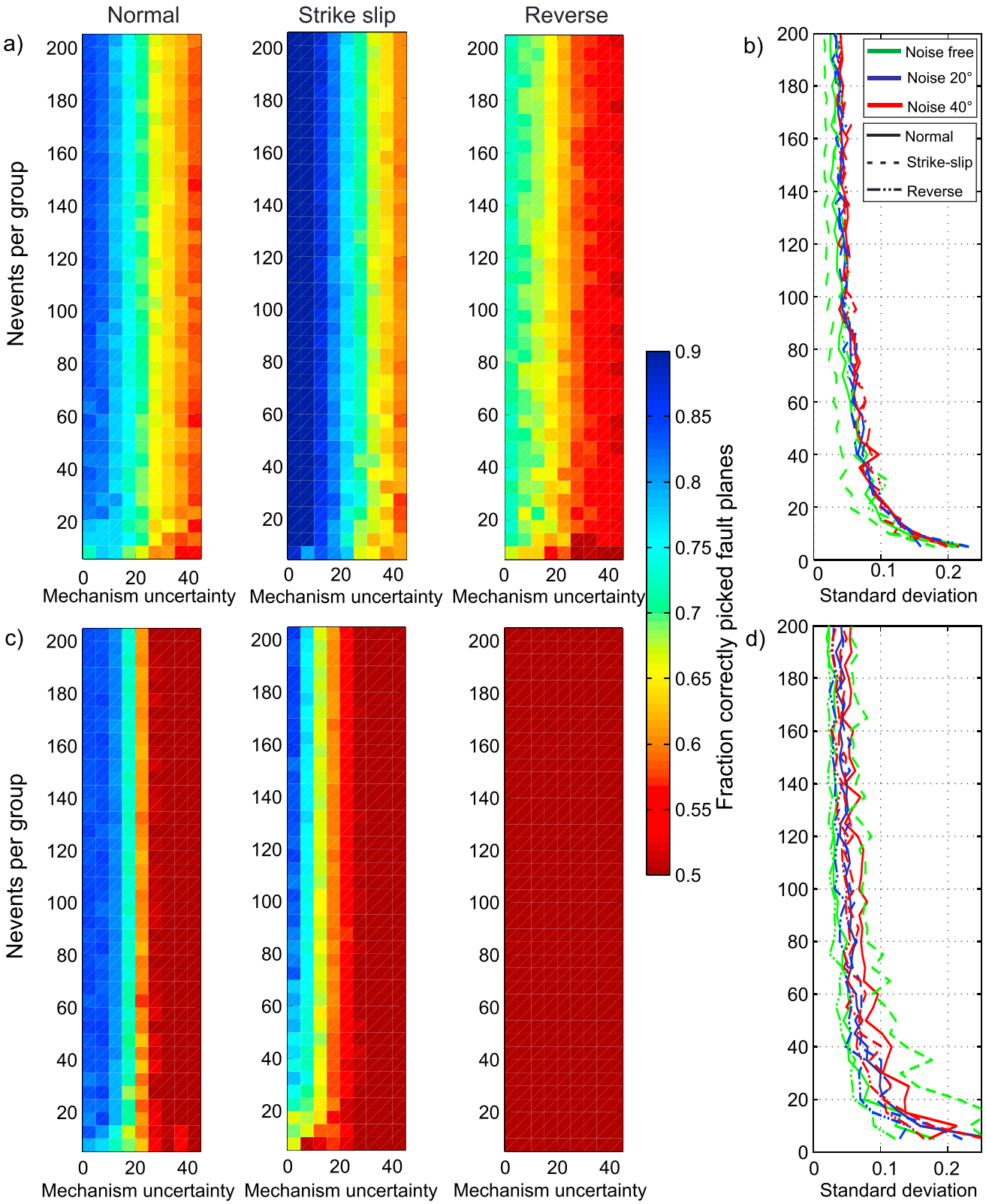

Figure 8. Fraction of correctly picked fault planes for normal, strike-slip, and reverse stress regimes and $R = 0.5$ using (a) the fault plane with highest instability and (c) the fault plane with lowest slip misfit angle. (b) Standard deviations of the fraction of correctly picked fault planes using the instability criterion in 50 realizations with different noise conditions. (d) Same as Figure 8b using the slip misfit criterion.

5. Case Study: Subset of Seismicity From the SJFZ

To illustrate the performance of the discussed stress inversion methodology, we utilize the 2010 seismicity from a portion of the SJFZ. The declustered catalog is discretized into 30 groups of seismicity containing between 30 and 60 focal mechanisms (section 3.3 and Figure 6), and the groups are organized in a grid of 53×4 nodes (section 4.1 and Figure 7). These groups of focal mechanisms are inverted for the stress field orientation and stress ratio following the methodology outlined in section 4.3. Figure 9 presents results from a stress inversion selecting the fault planes according to the highest instability and without damping (i.e., using a damping parameter value $d = 0$). The results consist of map views with 30 stress field orientations (Figure 9a) and stress ratio estimates (Figure 9b). The spatial variations of the results without damping contain some strong changes at adjacent regions, particularly in the stress ratio. Figure 10 shows corresponding results adding the use of a damping least squares inversion with a damping factor $d = 2$ selected from minimizing the data variance and model length. In this case, the larger variations between adjacent regions are smoothed. We therefore prefer in this case the results of Figure 10 using the damped least squares inversion on those of Figure 9. The inversion utilizes a regular grid, but the stress estimates are distributed irregularly in space and reflect the actual seismicity used in the different regions. Areas with higher seismic density are more finely discretized, and they generally show stress field orientations that are highly consistent with each other. The orientation of the maximum horizontal stress [*Lund and Townend*, 2007] calculated with the damped least squared inversion displays smaller uncertainty (Figures 9a and 10a). A small area around longitude-latitude coordinates [−116.6°, 33.45°] is observed to contain normal faulting stress regime only in the inversion without damping. The maximum horizontal stress is generally oriented in the north-south direction in agreement with the overall orientation of the maximum horizontal stress in Southern California [*Yang and Hauksson*, 2013]. However, at latitudes $> 33.5°$ the inverted maximum horizontal stress has a NNE trend, and at lower latitudes many of the inversions show orientations toward the NNW (Figure 10a).

Using the results of the damped inversion, we classify different stress regimes based on the plunge angles of the stress axes [*Zoback*, 1992]. We find that 12 subregions are associated with a strike-slip stress regime, while 18 have an oblique regime. Oblique slip on small faults in the region can reflect failure in a relatively strong crust adjacent to a mechanically weaker major fault [*Ghisetti*, 2000]. The examined section of the SJFZ has complex structure with two or three semiparallel major fault traces at the surface and significant rock damage between and around the traces [e.g., *Allam and Ben-Zion*, 2012; *Zigone et al*., 2015]. The areas with oblique strike-slip stress regime are mainly observed between the geological surface fault traces, while the areas with strike-slip regime are both between and outside the main fault traces. The maximum horizontal stress directions in the hot springs and trifurcation areas differ by about 10°, but in both regions they are oriented about 60–65° with respect to the main fault traces. These are in general agreement with previous estimations of σ_{HMAX} in the region [*Yang and Hauksson*, 2013] and the maximum compressive strain rate derived from GPS measurements [*Holt et al*., 2010; *Yang and Hauksson*, 2013]. The contrast in the patterns of R values across the SJFZ (Figures 9 and 10) is consistent generally with observed variations of shear wave anisotropy parameters across the fault [*Li et al*., 2015]. However, the fast propagation directions at various places on the NE side of the fault are significantly different than the direction of σ_{HMAX}. These discrepancies may be associated with the broad damage zone NE of the SJFZ [e.g., *Allam and Ben-Zion*, 2012; *Zigone et al*., 2015], and reduced stiffness normal to the damage zone observed at other locations [e.g., *Pischiutta et al*., 2012].

The stress ratios are overall consistent between nearby discretized groups, but larger changes reaching ± 0.5 within adjacent regions are seen in the results without damping (Figures 9b and 10b). One observed tendency is a generally lower ($R < 0.5$) stress ratio in the region SE of Anza, and on average larger stress ratios ($R > 0.5$) in the region to the NW. The stress regime also varies slightly from strike slip to oblique. The distribution of fault planes (assuming the fault plane with highest instability to be correct) is also different within these two regions. In the NW portion most fault planes have strike oriented at 330°, in reasonable agreement with the general orientation of the SJFZ. However, in the SE portion a broader diversity of fault strikes is observed, with two sets of predominant fault planes oriented nearly perpendicular to each other at 225° and 350° (Figure 10a, insets). Another interesting trend is that the stress ratios of the discretized seismicity occurring on the SW side of the SJFZ tend to be lower than within the SJFZ or on the NE side.

To evaluate the relative influence of some inversion parameters on the final inversion results, we perform a new set of inversions modifying one condition at a time. In particular, we test the stress inversion results by

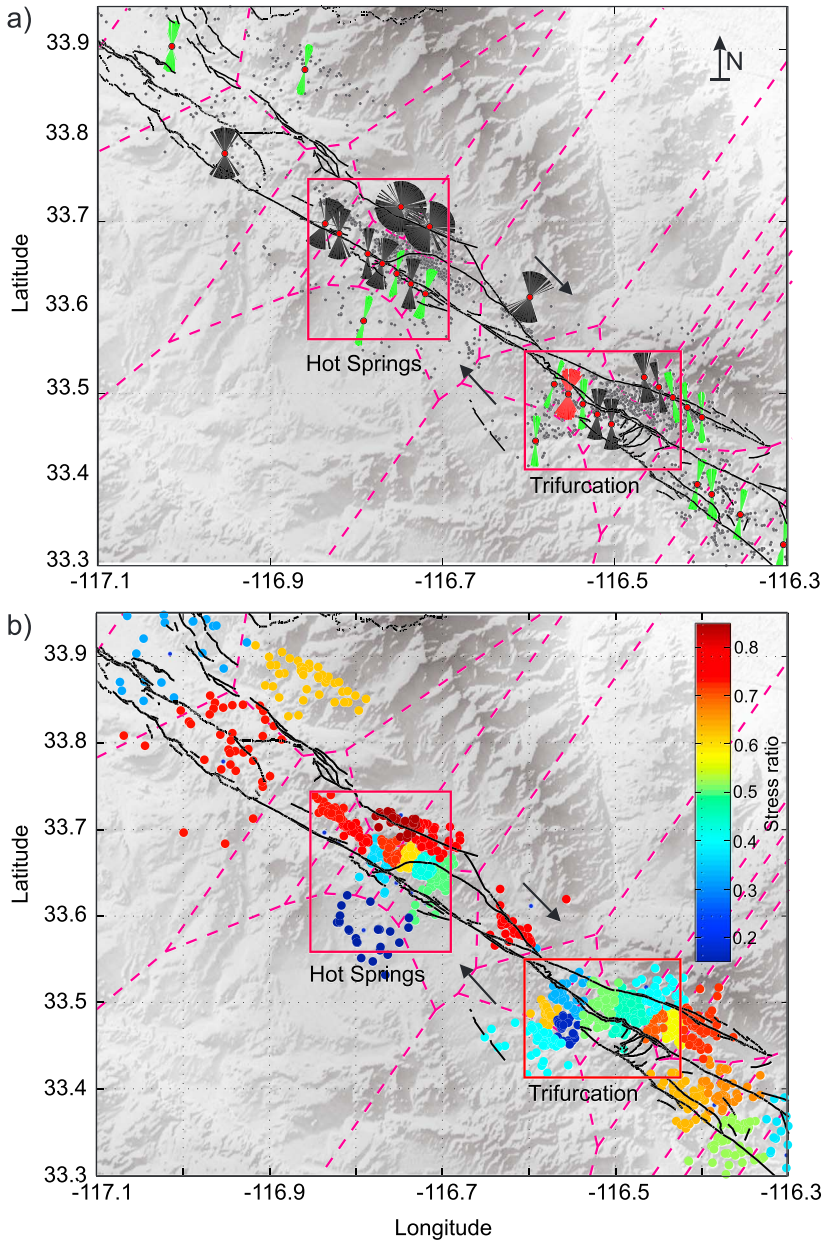

Figure 9. Stress inversion results with a damping parameter $d = 0$ for the obtained earthquake groups using a declustered catalog. Pink lines represent the used Voronoi cells. The black arrows indicate the orientation of the mean horizontal strain rate across the SJFZ (Community Geodetic Model, Southern California Earthquake Center, http://topex.ucsd.edu/CGM/CGM_html/). (a) Orientation of the maximum horizontal stress σ_{HMAX} following the estimation from *Lund and Townend* [2007]. Thickness of the symbols represent 95% confidence intervals derived from bootstrap resampling. Red filled circles mark the centroid of the corresponding earthquake groups. Green, red, and black symbols denote strike-slip, normal, and oblique stress regimes based on *Zoback* [1992]. (b) Seismicity used in each of the discretization groups is color encoded with the stress ratios derived from the inversion. Red rectangles mark the locations of the trifurcation and hot springs areas.

using a random fault plane choice, using the complete rather than declustered seismicity catalog, and grouping the seismicity with a different criterion. The obtained orientation of σ_{HMAX} is generally similar in most of these new inversion tests. Selecting the fault plane randomly has a minor effect in the inverted stress field orientation (Figure 11a), as already found by *Michael* [1987] and *Vavryčuk* [2014]. Using the complete seismicity catalog provides a substantially larger number of groups. The inverted stress field orientations are generally consistent, although in some areas (especially in the SE part) we observe rapid changes in the stress regime from oblique to strike slip (Figure 11b). This may be the result of including aftershocks, in particular of

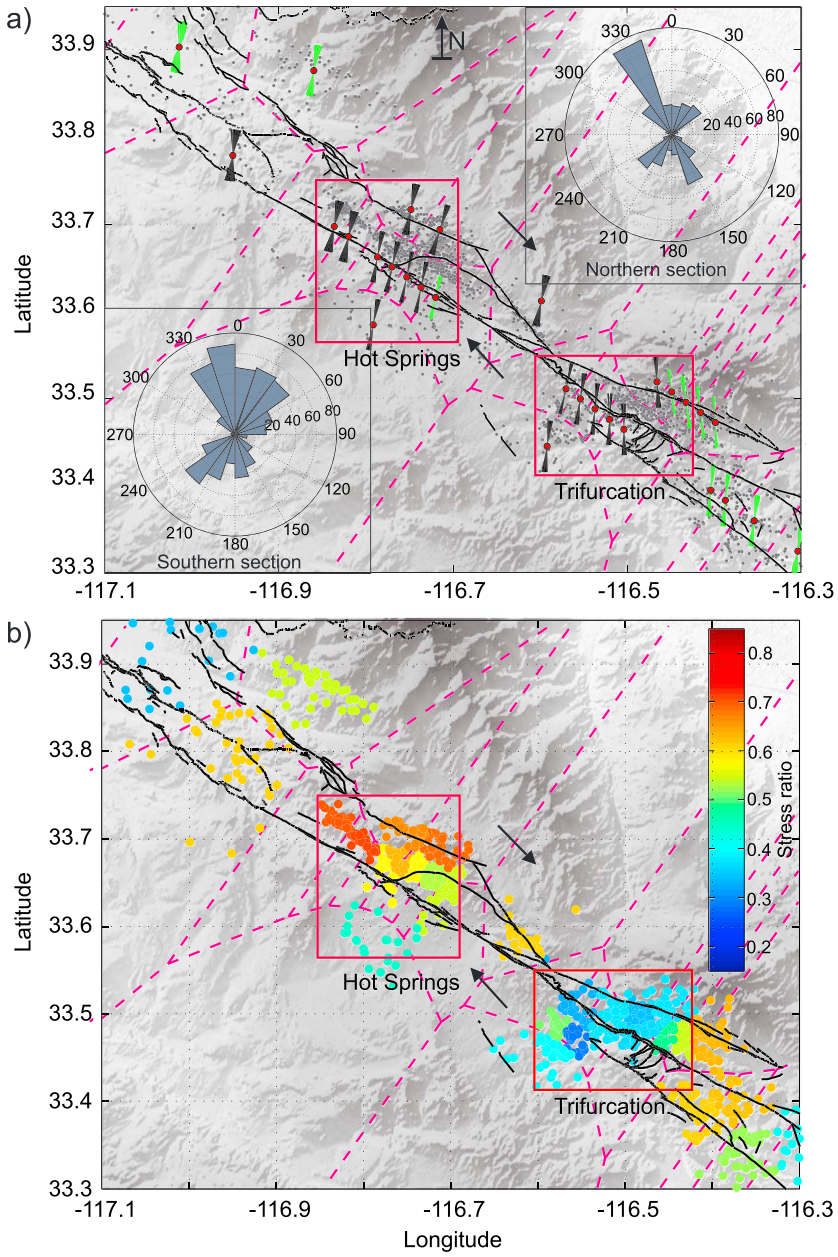

Figure 10. Stress inversion results with a damping parameter $d = 2$ for the obtained earthquake groups using a declustered catalog. (a) Orientation of the maximum horizontal stress σ_{HMAX} following the estimation from *Lund and Townend* [2007]. Thickness of the symbols represents 95% confidence intervals derived from bootstrap resampling. Red filled circles mark the centroid of the corresponding earthquake group. Green, red, and black symbols denote strike-slip, normal, and oblique stress regimes based on *Zoback* [1992]. Top right and bottom left insets represent the distributions of the strikes of the fault plane selected from each focal mechanism using the instability criterion. "Northern" and "Southern" sections are separated by latitude 33.55°. (b) Seismicity used in each of discretization group color encoded with the inverted stress ratios. Red rectangles mark the locations of the trifurcation and hot springs areas.

the events with M_L between 4.9 and 5.5 (Figure 4). Finally, choosing arbitrary a grid of 10×10 km^2 reduces the number of stress estimates, since fewer regions have the required minimum number of focal mechanisms, and regions with higher seismicity are not further subdivided (Figure 11c).

The use of a random fault plane choice remarkably decreases the stress ratio, suggesting a mixed strike-slip and normal faulting environment along most places (Figure 12a). This may be an artifact of mixing correct and auxiliary fault planes in similar proportions. Using the complete catalog of seismicity (Figure 12b) leads

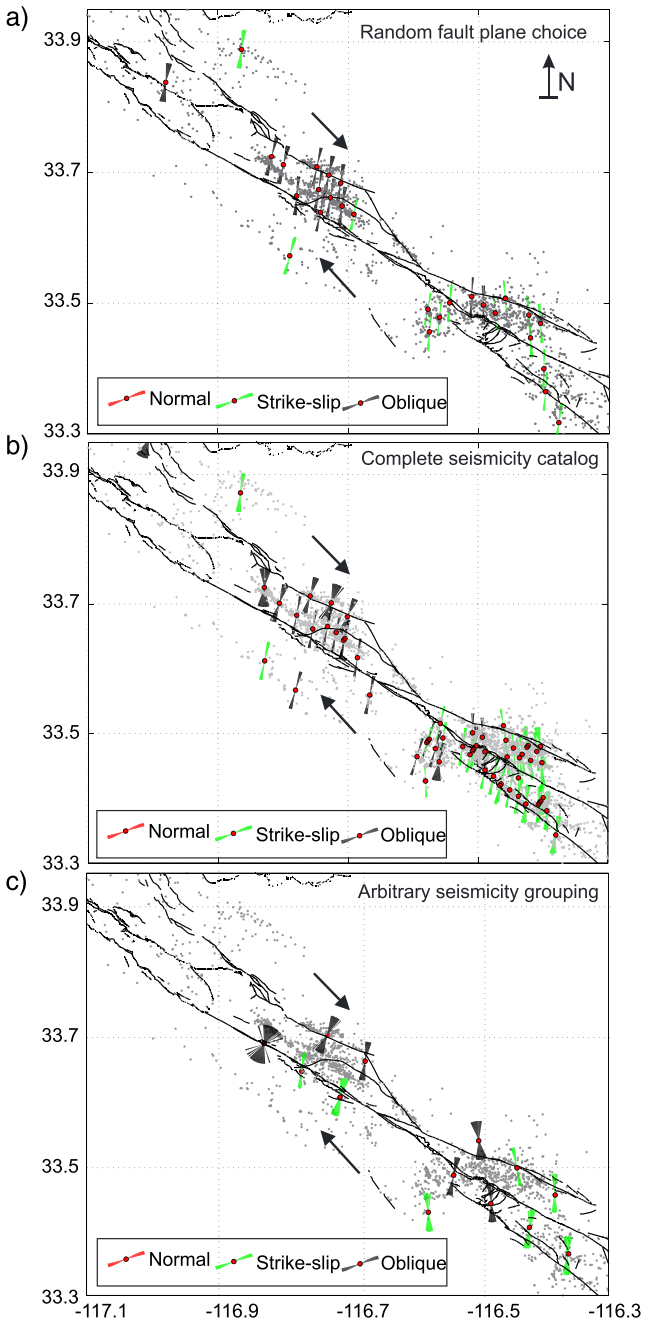

Figure 11. Distributions showing the maximum horizontal stress σ_{HMAX} orientation obtained by testing different nonoptimum inversion configurations. (a) Selecting randomly one of the fault planes in each focal mechanism. (b) Including aftershocks and foreshocks in the catalog. (c) Grouping the seismicity using regions of 10 km × 10 km.

to comparable stress ratios in most locations as in the preferred case of Figure 10. However, there are significant differences in the trifurcation area that includes the largest events (and their aftershock sequences). The stress ratios using an arbitrary grid of $10 \times 10\ km^2$ and without damping ($d = 0$) are comparable to the results using our discretization technique without damping (Figure 12c). However, the arbitrary discretization and associated arbitrary mixing of seismicity leads to reducing the differences in the stress ratios on the opposite sides of the fault that are observed in Figures 9 and 10. In summary, the inversion results tend to have larger heterogeneity at small scales in analyses with no damping and without catalog declustering. The results also

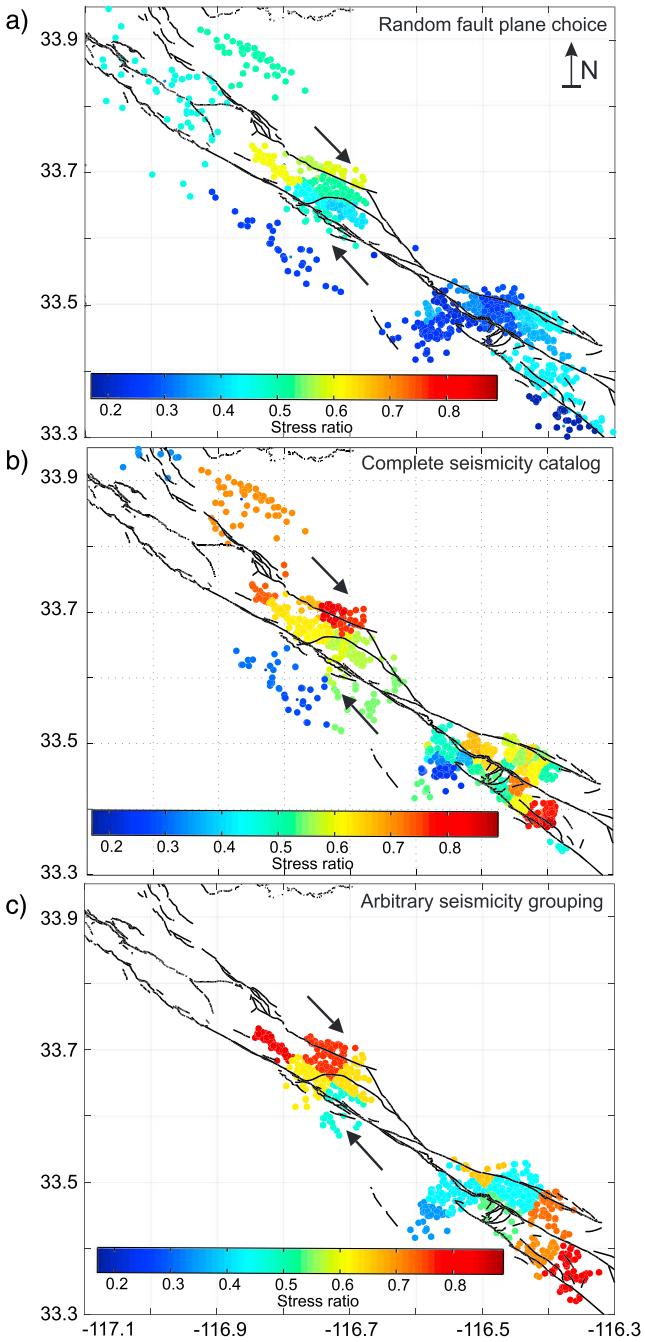

Figure 12. Stress ratios from the inversion configurations of Figure 11.

display unlikely homogeneity along areas of significant complexity in inversions with random selection of the fault planes. The refined stress inversion methodology leads with small damping ($d = 2$) to plausible results with generally consistent σ_{HMAX} and stress ratio at small scales, and large-scale variations that correlate with the geological structures (Figure 10).

6. Discussion and Conclusions

Many stress inversion studies have various arbitrary choices, particularly regarding the data selection. We propose a refined methodology to obtain stress distributions in two or three dimensions that incorporates several aspects of data selection and inversion steps (section 4.3). The data selection involves using

declustered seismicity and a minimum number of focal mechanisms that are found by synthetic tests to provide reliable results. These aspects of the methodology can be used with different inversion techniques. The main ingredients of the proposed inversion methodology are using iterative selection of the fault planes based on the instability criterion and comparing the stress field results obtained with and without the damping least squares technique as done in Figures 9 and 10 to achieve a balance between high resolution and lack of dependency of the results on the employed discretization.

As mentioned in section 1, various criteria are used to select a fault plane from each focal mechanism. From synthetic tests covering different stress regimes, stress ratios, and noise conditions, choosing the fault plane with the largest instability results in larger success rates (Figures 8, S6, and S7), although none of these criteria can ensure a completely correct selection of fault planes. The slip misfit criterion is less accurate than the instability criterion for cases with higher noise. These results are in good agreement with previous synthetic tests as well as analysis based on a data set of slickensides [*Lund and Slunga*, 1999]. The accuracy of the inversion results depends on the noise conditions and the existing stress state. From synthetic tests selecting fault planes using the instability criterion, we estimate that for cases with stress ratios $R = 0.5$, at least 20 (noise-free data) and 40 (for data with up to $\approx 40°$ of uncertainty) focal mechanisms are needed to achieve accuracies of $\pm 10°$ and ± 0.1 in the stress field orientation and R, respectively. However, higher number of focal mechanisms are required if the R values are near the extremes [0, 1]. These numbers are in relatively good agreement with those suggested in previous synthetic tests investigating the stress inversion accuracy [*Hardebeck and Hauksson*, 2001b; *Vavryčuk*, 2015]. The fault plane uncertainties explored here are intended to account primarily for observational errors, but they may also represent errors associated with the inversion process. These include deviations from the Wallace-Bott criterion, wrong fault plane choice, and non-double-couple source components.

We show that performing stress inversions with standard (not declustered) seismicity data can lead to clear temporal and spatial variations of inverted parameters of the stress field, especially around the space-time domains that include relatively large events (and their aftershock sequences). Using a declustered seismicity catalog can provide better estimates of the background stress field. Declustering the catalog reduces the number of focal mechanisms available for inversion, but the remaining data are more consistent with the assumption of homogeneous stress field within each region containing the events used in the inversion. An objective selection of event groups to be inverted for stress parameters is provided by the presented discretization method based on the *k*-means algorithm. This technique uses by default the normalized Cartesian distance between events, but time may be added if desired. An application to seismicity in the SJFZ area illustrates that the method produces naturally groups of events that are correlated with the surface traces of the main faults and regions of complexity. The size of the discretization in space (or time) is variable in relation to the seismicity density. This makes the technique less prone to mix areas governed by different local stress fields. However, regions with lower seismicity density will result in relatively larger areas which accordingly may potentially contain larger stress heterogeneity. The results obtained for the SJFZ with a small damping parameter ($d = 2$) are consistent within small scales but exhibit clear changes of stress parameters to the NW and SE of Anza and on the opposite sides of the fault zone. More detailed analysis of stress parameters in the SJFZ with the refined inversion methodology will be the subject of a follow-up work.

Acknowledgments

The used seismicity and focal mechanism data for the SJFZ region are from *Hauksson et al.* [2012] and *Yang et al.* [2012], respectively. The software and synthetic focal mechanism catalogs used in this work can be obtained from the corresponding author (patricia@gfz-potsdam.de). We thank Ilya Zaliapin for discussions and tools for declustering seismicity and Vaclav Vavryčuk for help and feedback with the synthetic tests. P. M.G. acknowledges funding from the Helmholtz Association in the frame of the Helmholtz Postdoc Program. Y.B.Z. acknowledges support from the Department of Energy (award DE-SC0016520). The manuscript benefitted from useful comments by two anonymous referees.

References

Allam, A. A., and Y. Ben-Zion (2012), Seismic velocity structures in the Southern California plate-boundary environment from double-difference tomography, *Geophys. J. Int.*, *190*(2), 1181–1196, doi:10.1111/j.1365-246X.2012.05544.x.

Arnold, R., and J. Townend (2007), A Bayesian approach to estimating tectonic stress from seismological data, *Geophys. J. Int.*, *170*(3), 1336–1356, doi:10.1111/j.1365-246X.2007.03485.x.

Bailey, I. W., Y. Ben-Zion, T. W. Becker, and M. Holschneider (2010), Quantifying focal mechanism heterogeneity for fault zones in central and Southern California, *Geophys. J. Int.*, *183*(1), 433–450, doi:10.1111/j.1365-246X.2010.04745.x.

Ben-Zion, Y., and J. R. Rice (1993), Earthquake failure sequences along a cellular fault zone in a three-dimensional elastic solid containing asperity and nonasperity regions, *J. Geophys. Res.*, *98*, 14,109–14,131, doi:10.1029/93JB01096.

Bohnhoff, M., H. Grosser, and G. Dresen (2006), Strain partitioning and stress rotation at the North Anatolian fault zone from aftershock focal mechanisms of the 1999 Izmit $M_w = 7.4$ earthquake, *Geophys. J. Int.*, *166*(1), 373–385, doi:10.1111/j.1365-246X.2006.03027.x.

Bott, M. H. (1959), The mechanics of oblique slip faulting, *Geol. Mag.*, *96*, 109–117.

Gephart, J. W., and D. W. Forsyth (1984), An improved method for determining the regional stress tensor using earthquake focal mechanism data: Application to the San Fernando Earthquake Sequence, *J. Geophys. Res.*, *89*, 9305–9320, doi:10.1029/JB089iB11p09305.

Ghisetti, F. (2000), Slip partitioning and deformation cycles close to major faults in Southern California: Evidence from small-scale faults, *Tectonics*, *19*, 25–43, doi:10.1029/1999TC900054.

Hardebeck, J. (2010), Aftershocks are well aligned with the background stress field, contradicting the hypothesis of highly heterogeneous crustal stress, *J. Geophys. Res.*, *115*, B12308, doi:10.1029/2010JB007586.
Hardebeck, J. L., and E. Hauksson (1999), Role of fluids in faulting inferred from stress field signatures, *Science*, *285*(5425), 236–239, doi:10.1126/science.285.5425.236.
Hardebeck, J. L., and E. Hauksson (2001a), Crustal stress field in Southern California and its implications for fault mechanics, *J. Geophys. Res.*, *106*, 21,859–21,882, doi:10.1029/2001JB000292.
Hardebeck, J. L., and E. Hauksson (2001b), Stress orientations obtained from earthquake focal mechanisms: What are appropriate uncertainty estimates? *Bull. Seismol. Soc. Am.*, *91*(2), 250–262, doi:10.1785/0120000032.
Hardebeck, J. L., and A. J. Michael (2004), Stress orientations at intermediate angles to the San Andreas Fault, California, *J. Geophys. Res.*, *109*, B11303, doi:10.1029/2004JB003239.
Hardebeck, J. L., and A. J. Michael (2006), Damped regional-scale stress inversions: Methodology and examples for Southern California and the Coalinga aftershock sequence, *J. Geophys. Res.*, *111*, B11310, doi:10.1029/2005JB004144.
Hartigan, J. A., and M. A. Wong (1979), Algorithm AS 136: A *k*-means clustering algorithm, *J. R. Stat. Soc.*, *28*(1), 100–108.
Hauksson, E., W. Yang, and P. M. Shearer (2012), Waveform relocated earthquake catalog for Southern California (1981 to June 2011), *Bull. Seismol. Soc. Am.*, *102*(5), 2239–2244, doi:10.1785/0120120010.
Heidbach, O., M. Tingay, and F. Wenzel (2010), Frontiers in stress research, *Tectonophysics*, *482*(1–4), 1–2, doi:10.1016/j.tecto.2009.11.009.
Holt, W.E., E. Klein, and L.M. Flesch 2010. GPS strain rates, optimal fault slip rates, and predicted moment rates in Western U.S. Plate Boundary Zone, *Proceedings of the Workshop on Incorporating Geodetic Surface Deformation Data into UCERF3*, Palm Spring, Calif.
Ickrath, M., M. Bohnhoff, G. Dresen, P. Martínez-Garzón, F. Bulut, G. Kwiatek, and O. Germer (2015), Detailed analysis of spatiotemporal variations of the stress field orientation along the Izmit-Düzce rupture in NW Turkey from inversion of first-motion polarity data, *Geophys. J. Int.*, *202*(3), 2120–2132, doi:10.1093/gji/ggv273.
Jonhson, S. C. (1967), Hierarchical clustering schemes, *Psychometrika*, *2*, 241–254.
Kagan, Y. Y. (1991), 3-D rotation of double-couple earthquake sources, *Geophys J Int*, *106*, 709–716.
King, G. C. P., R. S. Stein, and J. Lin (1994), Static stress changes and the triggering of earthquakes, *Bull. Seismol. Soc. Am.*, *84*(3), 935–953.
Li, Z., Z. Peng, Y. Ben-Zion, and F. L. Vernon (2015), Spatial variations of shear wave anisotropy near the San Jacinto Fault Zone in Southern California, *J. Geophys. Res. Solid Earth*, *120*, 8334–8347, doi:10.1002/2015JB012483.
Lund, B., and R. Slunga (1999), Stress tensor inversion using detailed microearthquake information and stability constraints: Application to Ölfus in southwest Iceland, *J. Geophys. Res.*, *104*, 14,947–14,964, doi:10.1029/1999JB900111.
Lund, B., and J. Townend (2007), Calculating horizontal stress orientations with full or partial knowledge of the tectonic stress tensor, *Geophys. J. Int.*, *170*(3), 1328–1335, doi:10.1111/j.1365-246X.2007.03468.x.
Martínez-Garzón, P., G. Kwiatek, M. Ickrath, and M. Bohnhoff (2014), MSATSI: A MATLAB package for stress inversion combining solid classic methodology: A new simplified user-handling, and a visualization tool, *Seismol. Res. Lett.*, *85*(4), 896–904, doi:10.1785/0220130189.
Martínez-Garzón, P., V. Vavryčuk, G. Kwiatek, and M. Bohnhoff (2016), Sensitivity of stress inversion of focal mechanisms to pore pressure changes, *Geophys. Res. Lett.*, *43*, 8441–8450, doi:10.1002/2016GL070145.
McKenzie, D. P. (1969), The relation between fault plane solutions for earthquakes and the directions of the principal stresses, *Bull. Seismol. Soc. Am.*, *59*(2), 591–601.
Meng, X., and Z. Peng (2014), Seismicity rate changes in the Salton Sea Geothermal Field and the San Jacinto Fault Zone after the 2010 M_w 7.2 El Mayor-Cucapah earthquake, *Geophys. J. Int.*, *197*(3), 1750–1762, doi:10.1093/gji/ggu085.
Michael, A. J. (1984), Determination of stress from slip data: Faults and folds, *J. Geophys. Res.*, *89*, 11,517–11,526, doi:10.1029/JB089iB13p11517.
Michael, A. J. (1987), Use of focal mechanisms to determine stress: A control study, *J. Geophys. Res.*, *92*, 357–368, doi:10.1029/JB092iB01p00357.
Michael, A. J. (1990), Energy constraints on kinematic models of oblique faulting: Loma Prieta versus Parkfield-Coalinga, *Geophys. Res. Lett.*, *17*, 1453–1456, doi:10.1029/GL017i009p01453.
Michael, A. J. (1991), Spatial variations in stress within the 1987 Whittier Narrows, California, aftershock sequence: New techniques and results, *J. Geophys. Res.*, *96*, 6303–6319, doi:10.1029/91JB00195.
Michael, A. J., W. L. Ellsworth, and D. H. Oppenheimer (1990), Coseismic stress changes induced by the 1989 Loma Prieta, California Earthquake, *Geophys. Res. Lett.*, *17*, 1441–1444, doi:10.1029/GL017i009p01441.
Okada, Y. (1985), Surface deformation due to shear and tensile faults in a half-space, *Bull. Seismol. Soc. Am.*, *75*(4), 1135–1154.
Pischiutta, M., F. Salvini, J. Fletcher, A. Rovelli, and Y. Ben-Zion (2012), Horizontal polarization of ground motion in the Hayward fault zone at Fremont, California: Dominant fault-high-angle polarization and fault-induced cracks, *Geophys. J. Int.*, *188*(3), 1255–1272.
Ross, Z. E., and Y. Ben-Zion (2013), Spatio-temporal variations of double-couple aftershock mechanisms and possible volumetric earthquake strain, *J. Geophys. Res. Solid Earth*, *118*, 2347–2355, doi:10.1002/jgrb.50202.
Rousseeuw, P. J. (1987), Silhouettes: A graphical aid to the interpretation and validation of cluster analysis, *J. Comput. Appl. Math.*, *20*, 53–65, doi:10.1016/0377-0427(87)90125-7.
Scholz, C. H. (2002), *The Mechanics of Earthquakes and Faulting*, 2nd ed., Cambridge Univ. Press.
Seeber, G. A. F. (1984), *Multivariate Observations*, *John Wiley Sons Inc*..
Sibson, R. H. (1985), A note on fault reactivation, *J. Struct. Geol.*, *7*(6), 751–754, doi:10.1016/0191-8141(85)90150-6.
Townend, J., and M. Zoback (2001), Implications of earthquake focal mechanisms for the frictional strength of the San Andreas Fault system, *Geol. Soc. London Spec. Publ.*, *186*, 13–21, doi:10.1144/GSL.SP.2001.186.01.02.
Vavryčuk, V. (2011), Principal earthquakes: Theory and observations for the 2008 West Bohemia swarm, *Earth Planet. Sci. Lett.*, *305*(3–4), 290–296, doi:10.1016/j.epsl.2011.03.002.
Vavryčuk, V. (2014), Iterative joint inversion for stress and fault orientations from focal mechanisms, *Geophys. J. Int.*, *199*(1), 69–77, doi:10.1093/gji/ggu224.
Vavryčuk, V. (2015), Earthquake mechanisms and stress field, in *Encyclopedia of Earthquake Engineering*, edited by M. Beer et al., pp. 728–746 , Springer, Berlin Heidelberg.
Vavryčuk, V., F. Bouchaala, and T. Fischer (2013), High-resolution fault image from accurate locations and focal mechanisms of the 2008 swarm earthquakes in West Bohemia, Czech Republic, *Tectonophysics*, *590*, 189–195, doi:10.1016/j.tecto.2013.01.025.
Voronoi (1908), Nouvelles applications des paramètres continus à la théorie de formes quadratiques, *J Reine Angew Math*, *134*, 198–287.
Wallace, R. E. (1951), Geometry of Shearing Stress and Relation to Faulting, *J. Geol.*, *59*(2), 118–130.
Wesson, R. L., and O. S. Boyd (2007), Stress before and after the 2002 Denali fault earthquake, *Geophys. Res. Lett.*, *34*, L07303, doi:10.1029/2007GL029189.
Yang, W., and E. Hauksson (2013), The tectonic crustal stress field and style of faulting along the Pacific North America Plate boundary in Southern California, *Geophys. J. Int.*, doi:10.1093/gji/ggt113.

Yang, W., E. Hauksson, and P. M. Shearer (2012), Computing a large refined catalog of focal mechanisms for Southern California (1981–2010): Temporal stability of the style of faulting, *Bull. Seismol. Soc. Am.*, *102*(3), 1179–1194, doi:10.1785/0120110311.

Zaliapin, I., and Y. Ben-Zion (2013), Earthquake clusters in Southern California I: Identification and stability, *J. Geophys. Res. Solid Earth*, *118*, 2847–2864, doi:10.1002/jgrb.50179.

Zaliapin, I., and Y. Ben-Zion (2016), A global classification and characterization of earthquake clusters, *Geophys. J. Int.*, *207*(1), 608–634, doi:10.1093/gji/ggw300.

Zigone, D., Y. Ben-Zion, M. Campillo, and P. Roux (2015), Seismic tomography of the Southern California plate boundary region from noise-based Rayleigh and Love Waves, *Pure Appl. Geophys.*, *172*, 1007–1032, doi:10.1007/s00024-014-0872-1.

Zoback, M. L. (1992), First- and second-order patterns of stress in the lithosphere: The World Stress Map Project, *J. Geophys. Res.*, *97*, 11,703–11,728, doi:10.1029/92JB00132.